Nuclear Materials and Energy 27 (2021) 100961

Contents lists available at ScienceDirect

Nuclear Materials and Energy

journal homepage: www.elsevier.com/locate/nme

Cross diagnostics measurements of heat load profiles on the lower tungsten divertor of WEST in L-mode experiments

N. Fedorczak [a,*], J. Gaspar [b], Y. Corre [a], A. Grosjean [a], X. Courtois [a], J.P. Gunn [a], R. Mitteau [a], R. Dejarnac [c], J. Bucalossi [a], E. Tsitrone [a], T. Loarer [a], S. Brezinsek [d], the WEST team [1]

[a] CEA, IRFM, F-13108 Saint-Paul-Lez-Durance, France
[b] Aix Marseille Univ, CNRS, IUSTI, Marseille, France
[c] Institute of Plasma Physics, The Czech Academy of Sciences, Za Slovankou 3, 182 00 Prague 8, Czech Republic
[d] Forschungszentrum Jülich, Institut für Energie- und Klimaforschung Plasmaphysik, 52425 Jülich, Germany

ARTICLE INFO

Keywords:
Tokamak
Divertor
Heat flux
Diagnostics comparison
Infra-red
Thermocouples

ABSTRACT

WEST is a full metallic tokamak with an extensive set of diagnostics for heat load measurements. In this paper, heat loads on the lower divertor of WEST are investigated using two independent methods. A first method relies on the thermal inversion of temperature measurements from arrays of thermal sensors embedded a few millimeters below the surface, while the second consists in the inversion of black body surface temperatures measured by infra-red (IR) thermography. The challenge of IR based temperature measurements in the full metal environment of WEST is addressed through a simplified model, allowing to correct for global reflections and low surface emissivities of tungsten surfaces. A large database (> 100 L-mode discharges) is investigated. It is found that the energy absorbed by an outer divertor tile during a plasma discharge is closely estimated by the two diagnostics, over a large set of experimental conditions. A similar match is also found for the peak heat flux value on the outer target. The toroidal modulation of target heat loads by magnetic ripple is found to be consistent with the geometrical projection of a parallel heat flux component. Additionally, the heat flux channel width at the target is found to scale linearly with the magnetic flux expansion as expected. These observations give confidence in the robustness of the data from both diagnostics, and confirm the simple geometrical rules at use in the description of heat flux deposition on divertor targets. However, it is shown that the heat flux channel width estimated from infra-red thermography is about three times lower than the width estimated from embedded measurements, which is still under investigation.

1. Introduction

One of the primary task of the WEST tokamak is to test the actively cooled tungsten monoblock technology that will equip the lower divertor of ITER [1]. In a staged approach, the first version of the lower divertor consists in uncooled graphite tiles coated with tungsten [2], with a single toroidal sector of actively cooled tungsten monoblocks (30 degrees in toroidal direction). The first phase of the scientific exploitation of WEST resulted in stepwise progress in diverted plasma operation, with external heating power reaching 8 MW (combination of lower-hybrid current drive and ion cyclotron resonance heating), although plasma scenarios stayed generally limited to low confinement (L-mode) regimes due to the combination of strong toroidal magnetic field (3.7 T) and unmitigated radiation levels (about 50%). Nevertheless, estimations of deposited heat fluxes on the lower divertor reached peak values around 6 MW m^{-2} during L-mode scenarios with about 4 MW of heating power. The focus of this contribution is twofold: to detail how the deposited heat flux is estimated on the uncooled tungsten coated graphite tiles, and present a first parametric study of the peak heat flux deposited on the outer part of the lower divertor, including toroidal modulation by magnetic ripple and magnetic flux expansion at target. The estimate of deposited heat flux on the uncooled lower divertor of WEST is possible from several diagnostics: multiple arrays of flush mounted Langmuir probes [3], embedded thermocouples [4] and fiber Bragg gratings (FBG) [5], and finally infra-red thermography [6]. The latter is widely considered as the diagnostic of predilection for assessing the properties of deposited heat flux (amplitude and shape) on divertor targets and implement experimental scaling laws for future reactors [7]. That said, a full metal environment as in WEST shows

* Correspondence to: Cadarache center, Building 508, F-13108 Saint Paul Lez Durance, France.
E-mail address: nicolas.fedorczak@cea.fr (N. Fedorczak).
[1] See http://west.cea.fr/WESTteam.

https://doi.org/10.1016/j.nme.2021.100961
Received 28 September 2020; Received in revised form 29 January 2021; Accepted 3 March 2021
Available online 9 March 2021

important limitations in term of reflections [8] and surface emissivity [9,10], that are also foreseen in ITER [11]. On the other hand, the fiber Bragg grating diagnostic embedded in the divertor tiles of WEST offers an unprecedented spatial resolution of 12.5 mm along the poloidal direction, allowing an independent assessment of heat flux profile properties [12] without assumptions on reflections and surface emissivity. A careful comparison between results from infra-red thermography and embedded measurements is presented in this contribution. Comparison with Langmuir probes is in progress and will not be addressed here.

2. Experimental database

Experimental results discussed in this contribution are built from a series of 215 plasma discharges performed in WEST. These discharges consist in L-mode lower single null scenarios with heating powers from 1 MW to 8 MW (composed of ohmic, lower hybrid current drive and ion cyclotron resonance heating), featuring stationary phases of several seconds to allow for robust thermal analysis, toroidal magnetic field $B_T = 3.5$–3.7 T, plasma current from $I_P = 300$ kA to 800 kA (edge safety factor from $q_{95} = 7.7$ to 3.2), and finally various magnetic flux expansions at the divertor strike points. All the discharges are selected with respect to the existence of exploitable FBG measurements, and among them 112 discharges have exploitable infra-red measurements. For each discharge, deposited heat flux profiles are estimated in the middle of the stationary phase, and absorbed energies are estimated across the entire plasma phase. Magnetic reconstructions are performed by the code NICE [13] using magnetic and interfero-polarimetry measurement constrains.

Features of the heat loads on the WEST divertor will be compared to experimental scaling laws built from multi-machine databases. For L-mode conditions, we shall refer to the scaling laws of the heat flux channel width λ_q estimated along the outer target of JET and ASDEX-Upgrade by means of infra-red thermography [14]. For comparison, we shall also apply equivalent scaling laws built from H-mode conditions from six tokamaks [7]. The different scaling laws proposed in each work will serve to give ranges of predictions rather than unique values.

3. Infra-red thermography

WEST is equipped with a set of infra-red endoscopes located at the top of the chamber and dedicated to surveillance of the lower divertor components [6] with a spatial resolution in the range of 2.5 mm per pixel. The flat and open geometry of the WEST lower divertor makes the lines of sight of the endoscopes to be roughly orthogonal to the divertor surface and cover both inner and outer targets on the same view, as shown in Fig. 1. The top surface of tungsten coated graphite tiles are toroidally beveled by 1° in order to protect poloidal leading edges. Note that embedded thermal sensors (described in the following) are positioned in the volume beneath the exposed surface of each tile. Infra-red emission is filtered around 3.9 μm and the whole systems are absolutely calibrated to produce images in effective black-body temperature. These data are inverted into deposited heat flux using the TEDDY code [10]. The main limitations in this inversion are caused by the reflected luminance at low tile temperature, and the non uniform surface emissivity of divertor tiles. Note that we shall speak of *effective* reflection and emissivity in the following since it cannot be completely disentangled from uncertainties on calibration coefficients. The issues are in facts of two types. First, effective emissivities are found to be extremely low and highly inhomogeneous along single tiles, in particular around the main location of the magnetic strike point [10]. Second, these emissivity profiles are found to evolve across experimental campaigns [9], suggesting a finite sensitivity with surface states, for instance due to the evolution of co-deposited layers. Surface analysis of these coated graphite tiles is foreseen in a near future in particular to address the correlation of layer composition and thickness

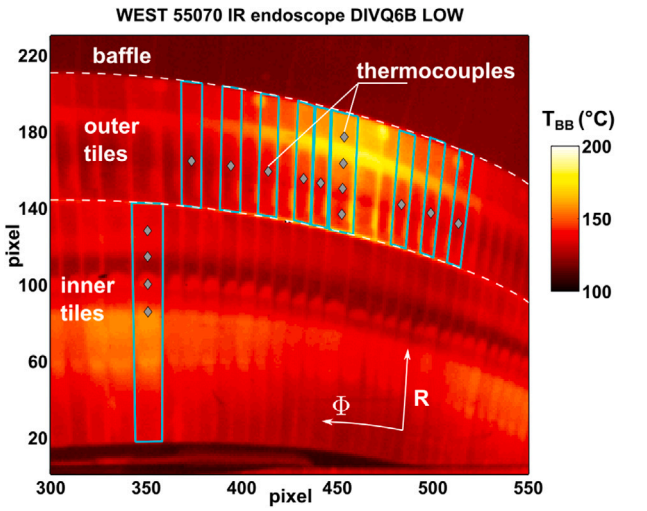

Fig. 1. infra-red view of a section of the lower divertor prior to a plasma pulse, following a session of divertor loading. The color-map represents the calibrated effective black body temperature. The pattern exhibits a toroidal modulation (along Φ) due to plasma loading modulated by magnetic ripple, and radial modulations (along R) consequent from varying surface emissivity. Light blue rectangles delimit tiles that are equipped with thermocouples, and along which treatments are performed. Tiles equipped with 4 thermocouples sits at toroidal locations where magnetic ripple produces the maximum deposited heat flux.

with surface emissivity. In order to perform a thermography inversion of a given experiment, surface emissivities and reflection coefficients need to be assessed at first. Since the tungsten coated graphite tiles are the main power exhaust components and they are not actively cooled, they gain finite temperature increments during each plasma pulse, that decay slowly but do not cancel at the beginning of the next pulse. This temperature increment is measured by thermocouples embedded in several tiles monitored by infra-red endoscopes. Since the remaining of the plasma chamber is actively cooled to a temperature of 90 °C, these temperature increments are the only cause of change of the infra-red image of the divertor prior to consecutive pulses (we shall indeed assume that emissivities do not change from pulse to pulse, but rather with a longer time scale). A procedure was implemented to estimate, for a given pulse, given infra-red endoscope and a given tile equipped with thermocouples, profiles of effective emissivity and background reflections. Note that reflections are simplified in the current state of the treatment: the luminance reflected by tiles is assumed to originate from the actively cooled chamber only, and is constant during plasma discharges. Self reflections are neglected, as reflections from other hot surfaces. This procedure, explained in [10], has been extended to entire campaigns. Results on emissivity evolution is the focus of a specific contribution [9]. For this work, we shall simply mention that this procedure is applied to infra-red data before implementing thermal inversions with TEDDY.

An illustration is given in Fig. 2, for an lower single null L-mode discharge featuring a stationary phase of about 20 s long, heated by 4 MW of lower hybrid current drive. The magnetic equilibrium drifts very slowly across that phase, causing a slow displacement of the magnetic strike points by about 6 mm. These features are also captured by the heat flux inversion: heat flux amplitudes are constant during the stationary phase of the discharge, and peak heat flux positions on both inner and outer tiles follow the strike point motion. Note on the profiles shown on the right panels of Fig. 2 that a systematic shift is found between magnetic strike point positions and heat flux profile centers, which is probably due to a systematic error in magnetic reconstruction. Nevertheless, this error is in the range of 10 mm and does not have a significant impact on the evaluation of magnetic properties around the peak heat flux location. Heat flux profiles are then analyzed

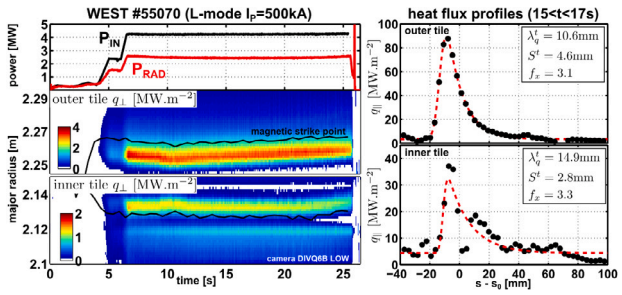

Fig. 2. Top left: time traces of injected power (lower hybrid current drive) and total radiated power. Below are shown the time evolution of the deposited heat flux on both outer and inner tiles (function of major radius). The magnetic strike points are shown as a black curve. Right: target profiles of incident parallel heat flux averaged around t = 16 s, function of the curvilinear coordinate of tiles (s_0 is the magnetic strike point position). The red dashed lines represent best fits, giving the two width parameters (S^t, λ_q^t) evaluated at target. The magnetic flux expansion at strike point (f_x) is also given.

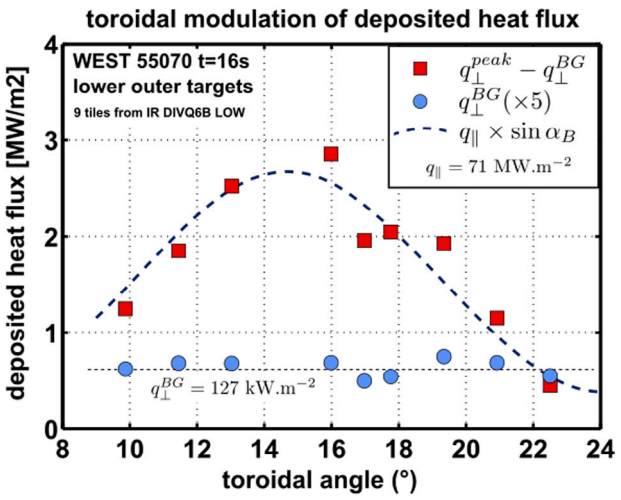

Fig. 3. Toroidal profiles of the peak (red squares) and background components (blue circles) of the deposited heat flux along 9 tiles sitting on the lower outer divertor (see Fig. 1). The dashed curve represents the geometrical projection of a uniform parallel heat flux, with α_B the incidence angle of the local magnetic field on the divertor surface.

following the same treatment procedure as implemented in [7] for constructing the H-mode multi-machine database on outer target heat flux width. Deposited heat flux are first projected along the direction of the magnetic field at target ($q_\perp \equiv q_\parallel \sin\alpha_B$). This approximation is discussed later. The parallel heat flux profile are then fitted along the curvilinear coordinate of the tile (s) following the formula describing the convolution of a Gaussian spreading with a truncated decaying exponential in the main scrape off layer domain:

$$q(\bar{s}) = \frac{q_0}{2} \cdot \exp\left(\left(\frac{S^t}{2\lambda_q^t}\right)^2 - \frac{\bar{s}}{\lambda_q^t}\right) \cdot \mathrm{erfc}\left(\frac{S^t}{2\lambda_q^t} - \frac{\bar{s}}{S^t}\right) + q_{BG}, \quad (1)$$

with q_0 the flux amplitude, q_{BG} a background amplitude, S^t the Gaussian spreading parameter along target, λ_q^t the heat flux channel width along target and $\bar{s} = s - s_0$ with s_0 the profile center position. As shown on the upper right graph of Fig. 2, the profile at the outer target is very well described by such a shape. Note that the Gaussian spreading is in the range of 40% of the exponential decay as commonly found in the multi-machine database [7], but it has to be noted that in the case of WEST treatments the instrumental function of the IR endoscope has not been corrected for, which necessarily contributes to this Gaussian spreading. The heat flux channel width at target λ_q^t can be remapped at midplane by removing the dependence with magnetic flux expansion around the strike point $\lambda_q \equiv \lambda_q^t / f_x$, which gives $\lambda_q = 3.4$ mm for this specific WEST L-mode discharge. For comparison, L-mode scaling laws give $\lambda_q = 3.3$–4.0 mm for this WEST scenario, whereas H-mode scaling laws give $\lambda_q = 1.3$–3.7 mm: The WEST point lies within L-mode predictions and two times H-mode predictions. The inner target exhibits a heat flux profile that is less coherent with the fit function due to the presence of multiple secondary peaks. In fact the profile seems to feature a hole about 10 mm outward of the peak position. This feature is not unique of WEST conditions (see for instance TCV observations [15]), and could be related to $E \times B$ flows in the scrape off layer [16], or a physical consequence of the presence of a second upper X-point in the chamber. The second separatrix strikes the inner target at $R \approx 2.08$ m thus a few centimeters away from the hole position. Nevertheless the effective heat flux channel width from the inner profile $\lambda_q = 4.5$ mm is not so far (by 30%) from the value along the outer one.

Last but not least, the intrinsic magnetic ripple of WEST is responsible for a toroidal modulation of the incidence angle of the magnetic field on the divertor, and consequently causes a toroidal modulation of the deposited heat flux. That said, the power deposited by radiation or charge exchange should be, at first order, independent of this ripple modulation which could be represented as a toroidally uniform background. Considering again the WEST experiment discussed above, profile analysis has been extended to the nine tiles of the outer target treated by the infra-red inversion. Both the peak deposited heat flux ($q_\perp^{peak}$) and flux background ($q_\perp^{BG}$) are evaluated by best fit with Eq. (1) and shown in Fig. 3, function of the toroidal angle. To be more precise, the background value has been subtracted from the peak value to account only for the plasma deposited part (note that the backgrounds are an order of magnitude smaller than the peak values). The toroidal modulation of these peak values is correctly reproduced by the geometrical projection of a toroidally uniform parallel heat flux on the divertor surface, with an RMS deviation of about 15%. This result validates the common assumption that the deposited heat flux can be approximated as the projection of a parallel heat flux, without significant contribution from a plasma flux transverse to the magnetic field. Additionally the background flux component is found to be insensitive to the magnetic field angle (with a statistical dispersion of about 10%), as one would expect for a non magnetized flux component (radiation and neutrals). The absolute magnitude of this background flux is $q_\perp^{BG} \approx 127$ kW m^{-2}. To compare with, a simplified tomography inversion of bolometry data is used to estimate the radiated power flux impacting the lower divertor, which gives $q_\perp^{rad} \approx 70$ kW m^{-2}. This value is a factor of about two lower than the background estimated from infra-red inversion, but it does not include the neutral charge exchange part that is at least partially screened form bolometers by the plasma itself.

4. Embedded diagnostics: TC and FBG

The WEST lower divertor is equipped with twenty thermocouples (TC) embedded 7.5 mm below the surface of uncooled tiles (see Fig. 1). Additionally, it is equipped with a novel type of thermal sensors also embedded in the uncooled graphite tiles. It consists in an optical fiber inserted in a lateral groove machined a few millimeters below the tile surface (3.5 mm or 7 mm), equipped with an array of FBG [12]. Each grating gives access to the local tile temperature evolution like embedded thermocouples, but with two important advantages: the optical system is not sensitive to electromagnetic interferences, and the spatial resolution of the system is enhanced thank to reduced spatial footprints. One the other hand, the time response of the thermal sensor is equivalent between thermocouples and gratings, mainly driven by the thermal contact of the sensor with the tile material (in the range of 250 ms). The fibers installed in WEST are each composed of 11 gratings spaced by 12.5 mm. The lower divertor of WEST is currently equipped

with four fibers embedded in outer target tiles at the toroidal positions of maximum ripple foot prints. These particular tiles are currently not monitored by infra-red thermography, so that comparison can only be done assuming that the 18 periods of ripple exhibit the same heat pattern. This is at least validated by the close match found between FBG and TC measurements from two distinct toroidal locations.

The spatial resolution of the FBG allows for a thermal inversion of local temperatures into a deposited heat flux at the surface of the tiles. The inversion is however ill-posed because sensors are embedded a few millimeters below the surface. The current inversion algorithm [12] is constrained by imposing a shape function to the deposited heat flux, given by Eq. (1). This shape depends on five parameters: the background value (q_{BG}), the amplitude value (q_0), the central position (s_0), the Gaussian spreading factor (S^t) and the heat flux channel width (λ_q^t). In principle, these five parameters shall evolve in time across a plasma discharge, but discharges considered in this work feature long stationary phases over which most of the parameters can be considered as constant. The current description of the heat flux pattern in the FBG inversion is as follow: both background and amplitude are unknown and allowed to evolve in time to account for the dynamics of input and radiated power, the heat flux channel width and central position are unknown but constant in time, and the Gaussian spreading is prescribed as a constant $S^t = 5$ mm. This last assumption is dictated by the fact that this spreading factor is generally smaller than the distance between two sensors, which would make the inversion too sensitive. This value of 5 mm has been selected to be in the range of what is usually measured by the IR inversion. Nevertheless, a sensitivity study on synthetic data showed that even if this spreading factor is not right, the inversion returns the right heat flux decay length λ_q^t within 10% accuracy. Similarly, assuming that the position of the profile center s_0 is constant in time may not be generally true as shown in Fig. 2. Again, a sensitivity study showed that the center position estimated by the inversion coincides with the time average of the true position, without noticeable impact on the estimate of the heat flux decay length. This inversion method is applied to FBG located at outer tiles, but also to thermocouple data located at the inner tile. Although the thermocouple array is composed of only 4 TC with a spatial resolution of 37.5 mm, it was shown that such an inversion method can give reliable estimates of heat flux profiles [4].

Considering the plasma pulse discussed in the previous Fig. 1, a quantitative comparison of the inverted heat fluxes from IR and embedded sensors is shown in Fig. 4. At both targets, the two inversions give similar peak heat flux amplitudes and a similar peak position. Nevertheless, a striking difference appears on the width of the profiles. Focusing on the outer target, the Gaussian spreading factors S^t are found to be quite close (4.8 mm from IR and 5 mm imposed for FBG), whereas the heat flux decay length estimated by FBG inversion is about 3 times higher than the value estimated from IR inversion. As we shall see in the following, such a disagreement persists across the selected database.

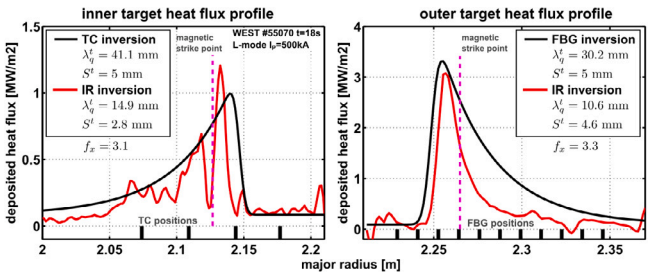

Fig. 4. Radial profiles of the deposited heat fluxes from embedded measurements and IR inversion along the inner and outer targets (at the maximum ripple modulation). Black curves show the TC (inner) and FBG (outer) inversions with the prescribed analytical shape and red curves are for the IR inversion. Absolute positions of the embedded sensors are shown as black ticks at the bottom of profiles. (For interpretation of the references to color in this figure legend, the reader is referred to the web version of this article.)

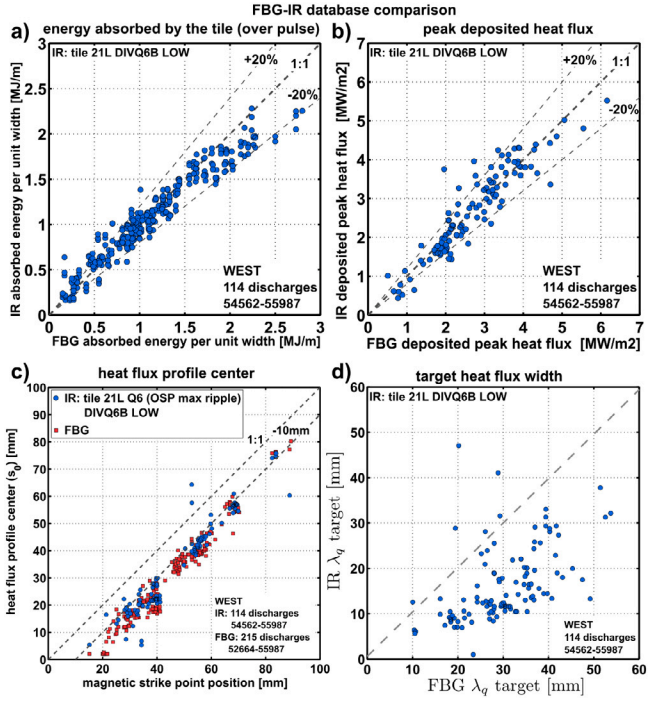

Fig. 5. Comparison of FBG and IR inversions for the outer tile across the WEST experimental database. (a) Linear energy absorbed by the tile during each discharge. (b) Peak heat flux during the stationary phase. (c) Center of the profiles (estimated by best fit) function of the magnetic strike point position (calculated by the code EQUOINOX). (d) Heat flux channel width at target.

5. Database comparison between FBG and IR

The comparison between FBG and IR estimates of heat fluxes is now extended through a database presented in Section 2. Because the shape of IR flux profiles along the inner target are not yet understood correctly, the comparison will focus on the outer tile at maximum ripple modulation where the FBG are installed, following a staged approach starting from global quantities up to shape parameters of the heat flux patterns. Considering that the FBG heat flux treatment is limited by a prescribed heat flux shape and a slow time response (compared to IR treatment), the most global observable on which both diagnostics should agree on is the integral of the heat flux pattern. For that purpose we define an integral observable, the linear energy E_l absorbed by the tile:

$$E_l \equiv \int_t \int_s q_\perp(s) ds \tag{2}$$

The deposited heat flux is integrated along the tile coordinate (power per unit length) and then integrated along the entire discharge duration so that E_l has the unit of [J m^{-1}]. The double integral ensures that detailed spatio-temporal properties are smoothed out. In fact, one may realize that this absorbed energy is directly linked to the temperature increment of the tile at the end of the discharge, so that it can be considered as a robust observable from FBG measurements. On the other hand, the surface temperature measured by IR is rather subject to an approximate effective emissivity treatment. The estimates of this linear energy by the two diagnostics are compared in Fig. 5a. A quantitative agreement is found over one decade from 0.2 MJ m^{-1} to 3 MJ m^{-1}, with a dispersion in the range of 20%. In fact it seems that the IR estimate may start falling systematically below the FBG estimate above 2 MJ m^{-1}. It might be a statistical bias from the database, that needs to be enlarged with additional long pulse discharges, or this may come from biases in the IR treatment. Effective emissivity profiles are

estimated at surface temperatures around or below 200 °C, whereas uncooled tile surfaces can reach above 1000 °C during long pulses. Tungsten surface emissivities in the infra-red range are generally measured to increase very weakly with surface temperature, as shown for the WEST tiles [17]. In any case this dependence is not considered here, so that effective emissivities at use in the IR treatment are globally underestimated during the heat deposition phase. This translates into an overestimation of surface temperature and thus an overestimation of deposited heat fluxes. Obviously this effect can only increase the difference between FBG and IR measurement, but rather marginally. The overall agreement on the linear energy suggest that the effective emissivities are possibly in the right range.

Comparison is now extended to the shape of the instantaneous heat flux profiles. To avoid any statistical biases from fine profile structures produced by the IR inversion, IR heat flux profiles are fitted with the shape function (Eq. (1)), that does also represent the shape imposed in the FBG heat flux inversion. Peak heat fluxes are compared in Fig. 5b. Again, a quantitative agreement is found over one decade, with a relative dispersion in the range of 20%. There is again a weak suspicion that IR estimates start to fall systematically below FBG ones for deposited heat fluxes above 5 MW m^{-2}, but this needs to be confirmed by additional experiments. Note also that all the discharges of this current L-mode database that show peak heat fluxes above 5 MW m^{-2} are externally heated with a total of 4 MW of lower hybrid current drive. These scenarios where operated with a magnetic flux expansion of about $f_x = 2$ at the outer target, which allowed for a concentrated heat deposition, whereas the average flux expansion across the database is about 4. In WEST scenarios, the magnetic flux expansion at target is simply changed by moving the X-point vertically with respect to the flat divertor. Doing so, the magnetic strike point moves along the outer target (and inner by symmetry). The commonly accepted physics behind the shape function of Eq. (1) is that the exponential decay of the scrape off layer profile is truncated at the magnetic strike point, whereas the private flux region is filled by the Gaussian spreading along the diverted magnetic leg. This means that the profile center s_0 that comes from the best fit of the profiles shall coincide with the magnetic strike point. Although drift effects could in principle cause a shift, this coincidence is for instance reported in lower single null TCV experiments [18]. Such a comparison is shown in Fig. 5c, for both IR and FBG profiles against the position of the magnetic strike point constructed by NICE. Agreement between FBG and IR profile positions is quantitative over a spatial range of 80 mm. The dispersion between the two diagnostics is in the range of a few millimeters, with a statistical relation reading $s_0^{\mathrm{FBG}} = s_0^{\mathrm{IR}} - 2.4$ mm $\pm$ 4.5 mm. The profile centers from both diagnostics follow quantitatively the magnetic strike point position, but with a systematic shift of about 10 mm over the whole range of positions. The statistical relation between FBG position and magnetic reads $s_0^{\mathrm{FBG}} = s_0^{\mathrm{mag}} - 14$ mm ± 3.5 mm. The shift is such that the heat flux profiles are shifted inward the private flux region with respect to the calculated magnetic separatrix. An explanation could come from a systematic error in the magnetic reconstruction, the plasma sitting at a lower vertical position than the reconstruction gives. Another possible explanation is an error in the definition of the absolute position of the tile as used presently.

Finally, the last comparison between FBG and IR heat fluxes presented in this contribution concerns the estimate of the heat flux channel width at outer target λ_q^t, as shown in Fig. 5d. This comparison shows a very large scatter over the range from 10 mm to 60 mm. Behind the scatter, it is also clear that the IR estimates of the heat flux channel width are smaller in amplitude than those estimated by FBG, by a factor of about 3. This global discrepancy covers the one mentioned earlier in Section 4.

This discrepancy is in fact persistent on a specific subset of the database. A set of reproducible discharges have been performed by scanning, from discharge to discharge, the magnetic flux expansion at target. Results on the heat flux channel width are shown in Fig. 6.

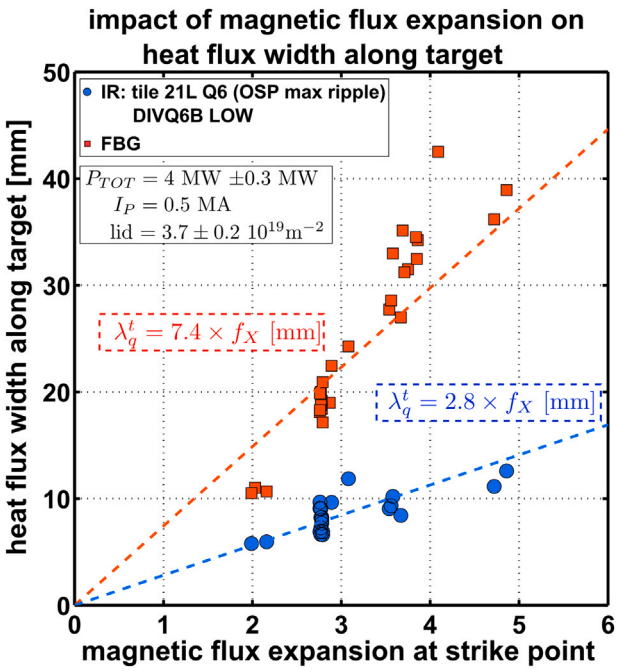

Fig. 6. Heat flux channel with λ_q^t at the outer target estimated by FBG (orange squares) and IR (blue circles) function of the magnetic flux expansion at the outer strike point. Each point corresponds to a single plasma discharge.

Both FBG and IR profiles give an estimate of λ_q^t that depends linearly on the magnetic flux expansion. This result is an important validation argument supporting the assumption that heat flux channel width at target can be remapped to midplane by a normalization with the magnetic flux expansion. A similar conclusion was obtained from TCV experiments [19]. On the other hand, it is very clear that the heat flux channel widths estimated by FBG are systematically 3 times higher than those estimated by IR. The linear trend between target width and flux expansion gives a global evaluation of the heat flux channel width remapped at midplane for these plasma conditions: $\lambda_q = 7.4$ mm from FBG and $\lambda_q = 2.8$ mm from IR. For comparison, L-mode scaling laws give $\lambda_q = 2.9$–3.7 mm and H-mode scaling laws give $\lambda_q = 1.1$–3.7 mm for these WEST scenarios: the IR estimated heat flux channel width is within L-mode predictions and within two times H-mode predictions.

6. Discussion and conclusion

The lower divertor of WEST is currently composed of a mix of actively cooled and uncooled plasma facing components, both covered by tungsten surfaces. These uncooled components are equipped with poloidal arrays of embedded thermal sensors, which are used to estimate deposited heat flux profiles from thermal inversion. Infrared thermography is also used to invert deposited heat flux profiles from surface temperature. In that case, a specific treatment needs to be done to make an effective correction of reflections inherent to full metal environments but also for inhomogeneities of tungsten surface emissivities. In the main strike point location of both inner and outer targets, the effective emissivity to apply to infra-red thermography falls in the range of $\epsilon \approx 0.1$ [9], which makes the correction mandatory in order to achieve quantitative thermography inversions. Corrections done, it results that infra-red thermography and embedded sensors return equivalent values of linear energy absorbed by an outer divertor target tile, over a large variety of plasma scenarios. This suggests that the emissivity correction for infra-red thermography is at least valid on average over the tile profile. Additionally, the peak heat flux inferred from both diagnostics are also equivalent over the database, which

suggests that emissivity is correct around the strike point location. Now, this agreement also remains when the strike point position is scanned over a large extend (80 mm), largely covering the main divertor area wetted during operation. It therefore suggests that emissivity profiles are correctly treated over the entire wetted area. Nevertheless, heat load profiles from embedded sensors and infra-red thermography strongly differ by the exponential width λ_q^t: values estimated from embedded sensors are about three times larger than estimated from infra-red thermography, with a large scatter (some cases show a good match). Note that infra-red values are in the range of predictions from L-mode scaling laws, also constructed from infra-red data. This discrepancy is still under investigation. Strikingly, such an agreement on the peak heat flux and difference on the heat flux width should result in a large difference in the linear energy, that is however not observed. In fact, the database shows that infra-red estimated heat flux backgrounds are about three times larger than backgrounds from embedded sensors. It results that backgrounds count for about 50% of the linear energy from infra-red profiles, but only 20% for embedded sensors. Such high background estimates from infra-red could be a consequence of an inappropriate treatment of reflections [8]. Let aside this pending but important issue, observations from WEST experiments are also validating key geometrical assumptions commonly followed in the description of deposited heat fluxes. Taking benefits of the magnetic ripple of WEST, the toroidal modulation of heat flux pattern is shown to be composed of a uniform background component (radiation and neutrals) and a modulated peak component that matches the geometrical projection of a pure parallel heat flux component. Finally, the heat flux channel width at target is found to be proportional to the magnetic flux expansion at target, validating the assumption that basic geometrical features along the divertor legs can be removed in order to construct remapped characteristic widths necessary for multi-machine comparisons. At low flux expansion, WEST L-mode scenarios are able to deposit, on the lower outer target, peak heat fluxes in the range of $q_\perp \approx 6$ MW m^{-2} with 4 MW of additional heating power. Improvement of radio-frequency power coupling and stabilization of high confinement modes should result in discharge scenarios delivering more than the $q_\perp \approx 10$ MW m^{-2} of deposited heat flux required to test ITER tungsten monoblocks in realistic heat exhaust conditions.

Declaration of competing interest

The authors declare that they have no known competing financial interests or personal relationships that could have appeared to influence the work reported in this paper.

Acknowledgment

Work performed under EUROfusion WP PFC. This work has been carried out within the framework of the EUROfusion Consortium and has received funding from the Euratom research and training programme 2014–2018 and 2019–2020 under grant agreement No 633053. The views and opinions expressed herein do not necessarily reflect those of the European Commission.

References

[1] J. Bucalossi, et al., Fusion Eng. Des. 89 (7) (2014) 907–912, Proceedings of the 11th International Symposium on Fusion Nuclear Technology-11 (ISFNT-11) Barcelona, Spain, 15-20 September, 2013.
[2] M. Firdaouss, C. Desgranges, C. Hernandez, M. Richou, H. Greuner, B. Böswirth, I. Zacharie-Aubrun, T. Blay, J. Bucalossi, M. Missirlian, F. Samaille, E. Tsitrone, Fusion Eng. Des. 124 (2017) 207–210, Proceedings of the 29th Symposium on Fusion Technology (SOFT-29) Prague, Czech Republic, September 5-9, 2016.
[3] R. Dejarnac, D. Sestak, J.P. Gunn, M. Firdaouss, H. Greuner, J-Y. Pascal, M. Richou, H. Roche, Fusion Eng. Des. 163 (2021) 112–120.
[4] J. Gaspar, Y. Corre, M. Firdaouss, J-L. Gardarein, D. Guilhem, M. Houry, C. Le Niliot, M. Missirlian, C. Pocheau, F. Rigollet, J. Phys. Conf. Ser. 745 (2016) 032091.
[5] Y. Corre, G. Laffont, C. Pocheau, R. Cotillard, J. Gaspar, N. Roussel, M. Firdaouss, J.-L. Gardarein, D. Guilhem, M. Missirlian, Rev. Sci. Instrum. 89 (6) (2018) 063508.
[6] X. Courtois, M.H. Aumeunier, C. Balorin, K. Blanckaert, M. Houry, M. Jouve, P. Moreau, C. Pocheau, H. Roche, Fusion Eng. Des. 136 (2018) 1499–1504, Special Issue: Proceedings of the 13th International Symposium on Fusion Nuclear Technology (ISFNT-13).
[7] T. Eich, A.W. Leonard, R.A. Pitts, W. Fundamenski, R.J. Goldston, T.K. Gray, A. Herrmann, A. Kirk, A. Kallenbach, O. Kardaun, A.S. Kukushkin, B. LaBombard, R. Maingi, M.A. Makowski, A. Scarabosio, B. Sieglin, J. Terry, A. Thornton, ASDEX Upgrade Team and JET EFDA Contributors, Nucl. Fusion 53 (9) (2013) 093031.
[8] Charly Talatizi, Marie-Hélène Aumeunier, Fabrice Rigollet, Mickael Le Bohec, Jonathan Gérardin, Jonathan Gaspar, Christophe Le Niliot, Albrecht Herrmann, Fusion Eng. Des. 159 (2020) 111867.
[9] J. Gaspar, M.-H. Aumeunier, M. Le Bohec, F. Rigollet, S. Brezinsek, Y. Corre, X. Courtois, R. Dejarnac, M. Diez, L. Dubus, N. Fedorczak, M. Houry, V. Moncada, P. Moreau, C. Pocheau, C. Talatizi, E. Tsitrone, Nucl. Mater. Energy 25 (2020) 100851.
[10] N. Fedorczak, J. Gaspar, M. Firdaouss, V. Moncada, A. Grosjean, R. Dejarnac, S. Brezinsek, E. Tsitrone, J. Bucalossi, T. Loarer, and, Phys. Scr. T171 (2020) 014046.
[11] M.-H. Aumeunier, M. Koan, R. Reichle, E. Gauthier, Nucl. Mater. Energy 12 (2017) 1265–1269, Proceedings of the 22nd International Conference on Plasma Surface Interactions 2016, 22nd PSI.
[12] J. Gaspar, Y. Corre, J-L. Gardarein, M. Firdaouss, D. Guilhem, M. Houry, G. Laffont, C. Le Niliot, M. Missirlian, C. Pocheau, F. Rigollet, Nucl. Mater. Energy 12 (2017) 1077–1081, Proceedings of the 22nd International Conference on Plasma Surface Interactions 2016, 22nd PSI.
[13] Blaise Faugeras, Francesco Orsitto and, Nucl. Fusion 58 (10) (2018) 106032.
[14] A. Scarabosio, T. Eich, A. Herrmann, B. Sieglin, J. Nucl. Mater. 438 (2013) S426 – S430.
[15] G.P. Canal, T. Lunt, H. Reimerdes, B.P. Duval, B. Labit, W.A.J. Vijvers, and, Nucl. Fusion 55 (12) (2015) 123023.
[16] V. Rozhansky, P. Molchanov, I. Veselova, S. Voskoboynikov, A. Kirk, D. Coster, Nucl. Fusion 52 (10) (2012) 103017.
[17] J. Gaspar, C. Pocheau, Y. Corre, N. Ehret, D. Guilhem, M. Houry, T. Loarer, Th. Loewenhoff, C. Martin, C. Pardanaud, G. Pintsuk, M. Richou, F. Rigollet, H. Roche, G. Sepulcre, M. Wirtz, Fusion Eng. Des. 149 (2019) 111328.
[18] A. Gallo, N. Fedorczak, S. Elmore, R. Maurizio, H. Reimerdes, C. Theiler, C.K. Tsui, J.A. Boedo, M. Faitsch, H. Bufferand, G. Ciraolo, D. Galassi, P. Ghendrih, M. Valentinuzzi, P. Tamain, and, Plasma Phys. Control. Fusion 60 (1) (2017) 014007.
[19] R. Maurizio, S. Elmore, N. Fedorczak, A. Gallo, H. Reimerdes, B. Labit, C. Theiler, C.K. Tsui, W.A.J. Vijvers, and, Nucl. Fusion 58 (1) (2017) 016052.